ELECTROCHEMISTRY

Single-site Pt-doped RuO_2 hollow nanospheres with interstitial C for high-performance acidic overall water splitting

Juan Wang[1,2]†, Hao Yang[3]†, Fan Li[4]†, Leigang Li[1], Jianbo Wu[4,5,6], Shangheng Liu[1], Tao Cheng[3], Yong Xu[7]*, Qi Shao[3], Xiaoqing Huang[1]*

Realizing stable and efficient overall water splitting is highly desirable for sustainable and efficient hydrogen production yet challenging because of the rapid deactivation of electrocatalysts during the acidic oxygen evolution process. Here, we report that the single-site Pt-doped RuO_2 hollow nanospheres (SS Pt-RuO_2 HNSs) with interstitial C can serve as highly active and stable electrocatalysts for overall water splitting in 0.5 M H_2SO_4. The performance toward overall water splitting have surpassed most of the reported catalysts. Impressively, the SS Pt-RuO_2 HNSs exhibit promising stability in polymer electrolyte membrane electrolyzer at 100 mA cm^{-2} during continuous operation for 100 hours. Detailed experiments reveal that the interstitial C can elongate Ru-O and Pt-O bonds, and the presence of SS Pt can readily vary the electronic properties of RuO_2 and improve the OER activity by reducing the energy barriers and enhancing the dissociation energy of *O species.

INTRODUCTION

Electrocatalytic water splitting, which couples hydrogen evolution reaction (HER) at cathode and oxygen evolution reaction (OER) at anode, has been widely accepted as an important process for the production of hydrogen and the conversion of intermittent energy (*1*–*5*). Generally, the electrocatalytic water splitting can be operated in acidic, alkaline, and neutral conditions, and therefore, the performance is strongly dependent on the electrocatalysts (*6*–*11*). Compared to alkaline water splitting, water splitting in acidic media is critical for polymer electrolyte membrane (PEM) electrolyzer (*12*–*15*), which presents advantages including high gas purity and proton conductivity and small gas crossover, and therefore attracts great attention (*16*, *17*). However, a highly efficient water splitting in acidic media is limited by the disadvantages of sluggish reaction kinetics and harsh acidic and oxidative environments of OER (*18*–*20*). It is thus highly desired to develop robust electrocatalysts for acidic water splitting.

Despite the widespread applications of RuO_2 and IrO_2 for acidic OER (*21*–*23*), RuO_2 has been regarded as a promising catalyst for acidic OER because of its cheaper price and higher activity compared with IrO_2 (*24*, *25*). However, RuO_2 suffers from the drawback of poor stability in acidic media at high potential (*26*). Over the past decades, substantial efforts have been devoted to the modifications of RuO_2 to improve its stability for acidic OER (*27*–*29*). For example, it has been reported that Cu doping into RuO_2 hollow porous polyhedra can substantially improve the OER performance, and the catalyst displays excellent stability within 10,000 cyclic voltammetry (CV) cycles and 8-hour chronopotentiometric test (*30*). Shan *et al.* (*31*) demonstrated that the heterostructured Ru@IrO_x with a strong charge redistribution between strained Ru core and IrO_x shell can serve as a stable catalyst for acidic OER. Despite the fact that great progress has been achieved, the stability of RuO_2 in acidic conditions is still far away from the satisfaction for practical application. Therefore, the development of robust RuO_2-based catalysts for acidic OER is of great importance.

Here, we report that the single-site Pt-doped RuO_2 hollow nanospheres (SS Pt-RuO_2 HNSs) can be applied as high-performance electrocatalysts for overall acidic water splitting, in which the interstitial C is trapped in the gap while Pt replaces partial Ru sites in the form of single site. In particular, when SS Pt-RuO_2 HNSs were used as catalyst for water splitting in 0.5 M H_2SO_4, the required cell voltages are as low as 1.49, 1.59, and 1.65 V for reaching current densities of 10, 50, and 100 mA cm^{-2}, respectively, and their catalytic performance have surpassed most of the reported catalysts for overall water splitting. Detailed characterizations reveal that the presence of interstitial C can elongate Ru-O and Pt-O bonds in SS Pt-RuO_2 HNSs, and the introduced SS Pt strongly affects the electronic properties of RuO_2. Density functional theory (DFT) calculations show that the RuO_2 with SS Pt can significantly enhance the stability and reduce energy barriers for boosting OER activities. This work not only may provide a facile strategy for the modification of RuO_2 by doping SS Pt but also sheds new light on the industrial application of overall water splitting.

RESULTS

Morphological and structural characterizations

The PtRuSe HNSs was initially synthesized via a hydrothermal method, in which hydrazine hydrate aqueous solution and H_2O were used as

[1]State Key Laboratory of Physical Chemistry of Solid Surfaces, College of Chemistry and Chemical Engineering, Xiamen University, Xiamen 361005, China. [2]Key Laboratory of Carbon Materials of Zhejiang Province, College of Chemistry and Materials Engineering, Wenzhou University, Wenzhou 325035, China. [3]Institute of Functional Nano and Soft Materials (FUNSOM), Jiangsu Key Laboratory for Carbon-Based Functional Materials and Devices, Soochow University, Jiangsu 215123, China. [4]State Key Laboratory of Metal Matrix Composites, School of Materials Science and Engineering, Shanghai Jiao Tong University, Shanghai 200240, China. [5]Center of Hydrogen Science, Shanghai Jiao Tong University, Shanghai 200240, China. [6]Future Material Innovation Center, Zhangjiang Institute for Advanced Study, Shanghai Jiao Tong University, Shanghai 200240, China. [7]Guangzhou Key Laboratory of Low-Dimensional Materials and Energy Storage Devices, Collaborative Innovation Center of Advanced Energy Materials, School of Materials and Energy, Guangdong University of Technology, Guangzhou 510006, China.
*Corresponding author. Email: yongxu@gdut.edu.cn (Y.X.); hxq006@xmu.edu.cn (X.H.)
†These authors contributed equally to this work.

reducing agent and solvent, respectively. The obtained PtRuSe HNSs exhibit a morphology of HNS with a Pt/Ru/Se ratio of 4.7:31.6:63.7, as revealed by transmission electron microscopy (TEM) image and scanning electron microscopy–energy dispersive spectrometer (SEM-EDS) profile (fig. S1). The PtRuSe HNSs were then loaded onto the VC-X72 carbon powder (fig. S2). No obvious x-ray diffraction (XRD) peaks except for some typical bread-shaped diffraction peaks are observed, suggesting the amorphous nature of PtRuSe HNSs (fig. S3). Afterward, the carbon-supported PtRuSe HNSs were treated in air at 300°C for 10 hours to obtain SS Pt-RuO_2 HNSs. No obvious changes in the morphology were observed after this thermal treatment despite the fact that partial carbon was removed, as revealed by the high-angle annular dark-field scanning TEM (HAADF-STEM) (Fig. 1A) and TEM images (Fig. 1B). Results from SEM-EDS spectrum show that the atomic ratio of O/Ru/Pt/Se is 74.9:23.0:1.1:1.0 in SS Pt-RuO_2 HNSs, while the significant decrease of Se in SS Pt-RuO_2 HNSs is ascribed to the evaporation of Se during thermal treatment (fig. S4). The appearance of RuO_2 peaks and the absence of Pt peaks in the XRD pattern of SS Pt-RuO_2 HNSs indicate that Pt atoms are well dispersed on RuO_2 (Fig. 1C). In Raman spectra, the features of E_g, A_{1g}, and B_{2g} of RuO_2 are observed, and the disappearance of D-band and G-band of graphite carbon further confirms that the graphite structure is destroyed and RuO_2 is formed during the heat treatment process (fig. S5) (*32*). Spherical aberration–corrected HAADF-STEM measurement was performed to study the distributions of Pt atoms in SS Pt-RuO_2 HNSs. It is found that Ru atoms are partially replaced by Pt atoms in the form of isolated state (bright dots in Fig. 1D) (*33*, *34*). We further enlarged the selected area in Fig. 1D, and the details of the atomic line profiles further confirm the isolated state of Pt atoms in SS Pt-RuO_2 HNSs (Fig. 1, E to J). The corresponding fast Fourier transform (FFT) pattern of SS Pt-RuO_2 HNSs identifies the exposed (110) and ($\bar{1}$01) planes of RuO_2 along [$\bar{1}1\bar{1}$] zone axis (Fig. 1F), which suggests that Ru and O atoms are arranged with a tetragonal structure (*P42/mnm*) and Pt atoms are exclusively located at Ru position in the manner of single site (Fig. 1G). Moreover, STEM-EDS elemental mapping images suggest that all the elements are evenly distributed in SS Pt-RuO_2 HNSs (Fig. 1K). The absence of carbon shell in the high-resolution TEM (HRTEM) image implies that C has entered into RuO_2 (fig. S6). In addition, PtRuSe HNSs with different Pt atomic ratios were synthesized (denoted as RuO_2 HNSs, 2% Pt-RuO_2 HNSs, and 10% Pt-RuO_2 HNSs, respectively) (figs. S7 to S10). Similarly, the typical peaks of RuO_2 were observed in the XRD patterns and the Raman spectra of all samples. The presence of diffraction peaks of Pt in the XRD pattern of 10% Pt-RuO_2 HNSs suggests that Pt atoms present as nanoparticles

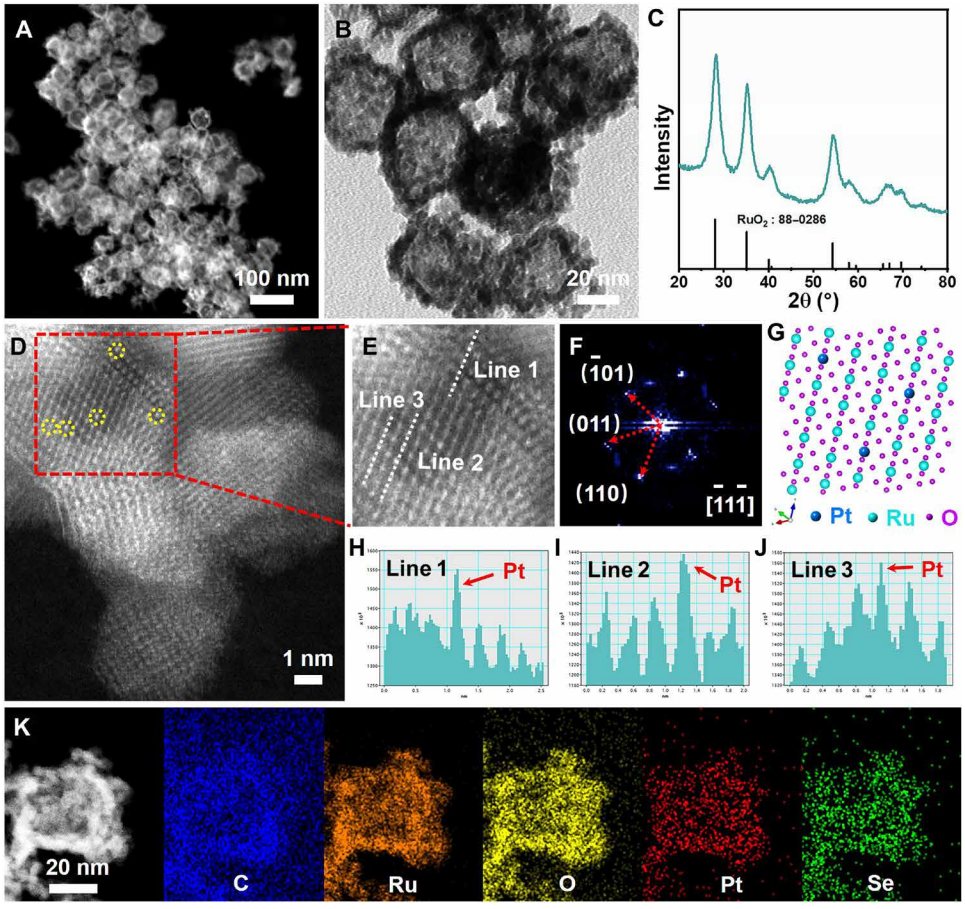

Fig. 1. Morphological and structural characterizations. (**A**) HAADF-STEM image, (**B**) TEM image, (**C**) XRD pattern, and (**D**) high-resolution HAADF-STEM image of SS Pt-RuO_2 HNSs. (**E**) High-resolution HAADF-STEM image obtained from the area highlighted with red rectangles in (D). (**F**) FFT pattern and (**G**) crystal structure model of SS Pt-RuO_2 HNSs. (**H** to **J**) Line-scanning intensity profile obtained from the area highlighted with white lines in (E). (**K**) STEM image and STEM-EDS elemental mapping images of SS Pt-RuO_2 HNSs.

(figs. S11 and S12). The lattice fringes in the HRTEM of 2% Pt-RuO_2 HNSs are ascribed to RuO_2 (101) and (110) planes, respectively (fig. S13). In addition to the lattice distances of RuO_2 (101) and (210) facets, the presences of Pt (111) and Pt (200) lattice distances in the HRTEM image of 10% Pt-RuO_2 HNSs further confirm the existence of Pt nanoparticles (fig. S14).

Catalytic performance

The OER and HER performance of various catalysts were evaluated in 0.5 M H_2SO_4 with standard three-electrode system. As shown in Fig. 2A, SS Pt-RuO_2 HNSs display small overpotentials of 228, 262, and 282 mV for achieving current densities of 10, 50, and 100 mA cm^{-2}, respectively, during OER. In contrast, the overpotentials are 325, 405, and 489 mV at the current densities of 10, 50, and 100 mA cm^{-2} when commercial RuO_2 was used as catalyst (table S1). Moreover, SS Pt-RuO_2 HNSs exhibit the smallest Tafel slope compared to RuO_2 HNSs and commercial RuO_2, suggesting the fastest reaction kinetics of SS Pt-RuO_2 HNSs for OER (Fig. 2B). To evaluate the OER activity, the overpotentials and Tafel slopes of various catalysts were summarized. It is found that SS Pt-RuO_2 HNSs exhibit significantly superior OER performance to RuO_2 HNSs and commercial RuO_2 (Fig. 2C). Moreover, when SS Pt-RuO_2 HNSs was used as catalyst for HER, the overpotentials are 26, 47, and 67 mV at the current densities of 10, 50, and 100 mA cm^{-2}, respectively, which are close to those values of the state-of-the-art Pt/C catalyst (Fig. 2D and table S2). By contrast, the overpotentials of RuO_2 HNSs are 68, 109, and 142 mV for achieving current densities of 10, 50, and 100 mA cm^{-2}, respectively. On the other hand, SS Pt-RuO_2 HNSs display a similar

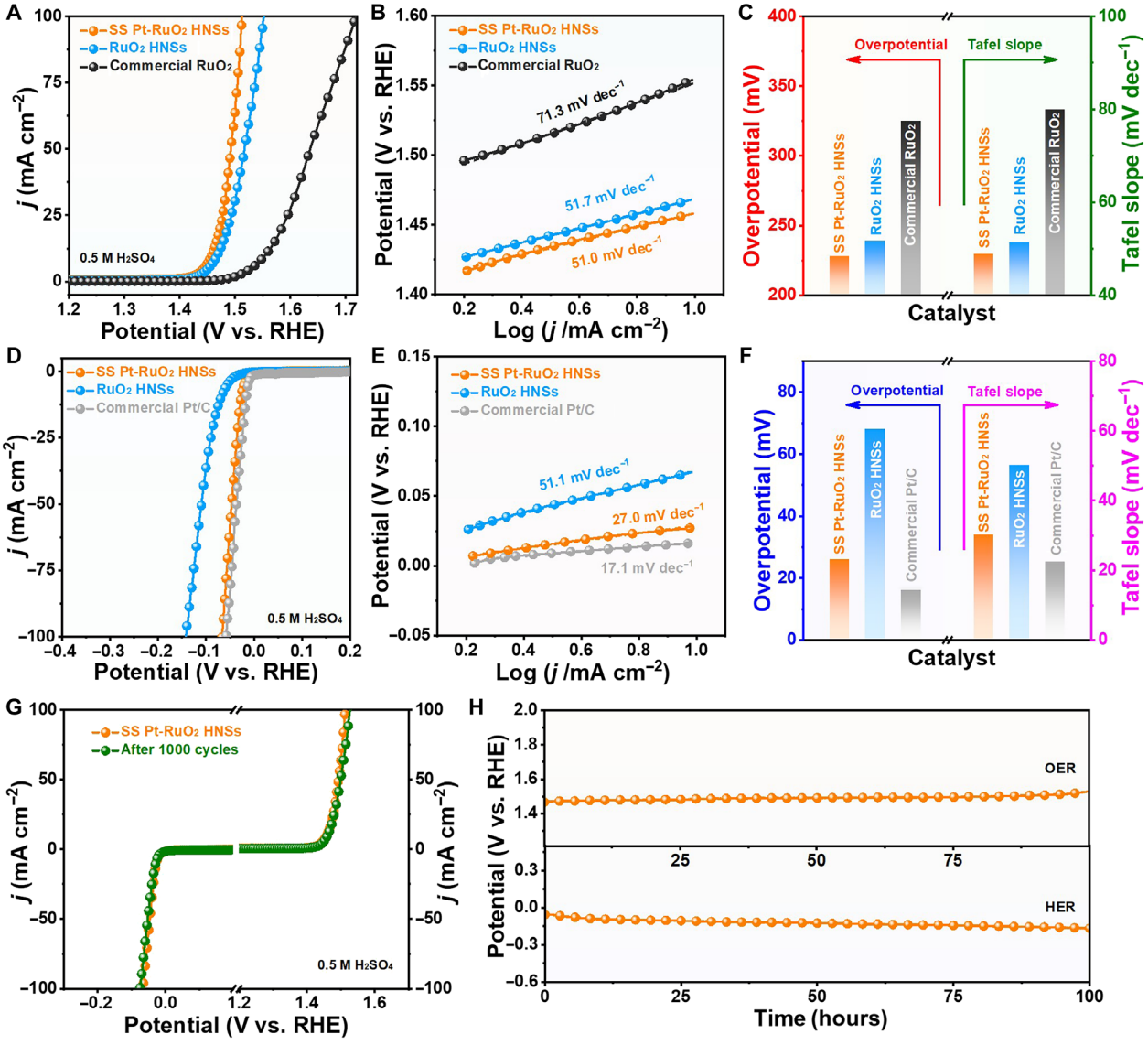

Fig. 2. Electrochemical OER and HER studies. (**A**) OER polarization curves and (**B**) corresponding Tafel slopes of SS Pt-RuO_2 HNS, RuO_2 HNSs, and commercial RuO_2. (**C**) Histogram of overpotentials at 10 mA cm^{-2} and Tafel slopes of various catalysts. (**D**) HER polarization curves and (**E**) corresponding Tafel slopes of SS Pt-RuO_2 HNS, RuO_2 HNSs, and commercial Pt/C. (**F**) Histogram of overpotentials at 10 mA cm^{-2} and Tafel slopes of various catalysts. (**G**) OER and HER polarization curves of SS Pt-RuO_2 HNS before (orange) and after (green) 1000 CV cycles. (**H**) Chronopotentiometry tests of SS Pt-RuO_2 HNS for OER and HER in 0.5 M H_2SO_4 at 10 mA cm^{-2}. RHE, reversible hydrogen electrode

Tafel slope to that of commercial Pt/C, further confirming the excellent HER activity of SS Pt-RuO_2 HNSs (Fig. 2, E and F). Moreover, the electrochemical active surface area of SS Pt-RuO_2 HNSs was evaluated by the double-layer capacitance (C_{dl}) from CV curves in the non-Faradaic region. It is found that the SS Pt-RuO_2 HNSs expose more active sites and therefore exhibit higher activity in comparison to RuO_2 HNSs (fig. S15). Furthermore, Pt-RuO_2 HNSs with different contents of Pt (e.g., 2 and 10%) were used as catalysts for OER and HER. It is noted that both 2% Pt-RuO_2 HNSs and 10% Pt-RuO_2 HNSs exhibit inferior activity and/or stability to SS Pt-RuO_2 HNSs (figs. S16 and S17). In addition, the slight decays in the OER and HER polarization curves after 1000 CV cycles imply the excellent electrocatalytic stability of SS Pt-RuO_2 HNSs (Fig. 2G). Chronopotentiometry tests for HER and OER were carried out at a constant current density of 10 mA cm^{-2} in 0.5 M H_2SO_4 to further investigate the stability of SS Pt-RuO_2 HNSs. For OER, the overpotential of SS Pt-RuO_2 HNSs remains stable for at least 100 hours, while the overpotential of commercial RuO_2 increases sharply after only ~2 hours, indicating the superior stability of SS Pt-RuO_2 HNSs to commercial RuO_2 (Fig. 2H and fig. S18). To demonstrate the significance of the interstitial C on the stability of SS Pt-RuO_2 HNSs, the PtRuSe HNSs were directly treated in air at 300°C for 10 hours without loading on VC-X72 carbon powder. It is noted that the hollow structure of PtRuSe HNSs is completely collapsed (fig. S19A), as a result of poor stability for OER (fig. S19B). The above results suggest the significance of interstitial C on the structural stability. In addition, we further investigated the influence of Se on both the structure and the stability for OER. In the absence of Se precursor (H_2SeO_3), only solid nanoparticles and amorphous carbon were observed after calcination in air at 300°C for 10 hours (fig. S20), indicating that Se plays a crucial role for the formation of SS Pt-RuO_2 HNSs. Besides, we further evaluated the effects of residual Se on the stability for OER through an electrochemical leaching process. As shown in fig. S21A, the atomic ratio of Se significantly decreases to 0.3% after the electrochemical leaching process. No obvious change of potential within 100 hours was observed (fig. S21B) compared to the SS Pt-RuO_2 HNSs without the electrochemical leaching process (Fig. 2H), indicating that the residual Se displays negligible effects on the durability test for OER. With respect to HER, the SS Pt-RuO_2 HNSs exhibits significantly improved stability in 100 hours compared to the commercial Pt/C (fig. S22).

Inspired by the excellent activity and long-term stability, the SS Pt-RuO_2 HNSs were simultaneously used as both cathode and anode catalysts in a two-electrode system for acidic overall water splitting (Fig. 3A). Notably, the SS Pt-RuO_2 HNSs show promising activity for overall water splitting, and the cell voltages are as low as 1.49, 1.59, and 1.65 V for achieving current densities of 10, 50, and 100 mA cm^{-2}, respectively (Fig. 3B). By contrast, the benchmark catalysts of commercial Pt/C for cathode and commercial RuO_2 for anode require a much larger cell voltage of 1.56, 1.67, and 1.77 V for reaching the same current densities. Moreover, the chronopotentiometry tests of SS Pt-RuO_2 HNSs||SS Pt-RuO_2 HNSs and commercial RuO_2||commercial Pt/C were performed in 0.5 M H_2SO_4 to evaluate their stability (Fig. 3C). The required cell voltage for commercial RuO_2||commercial Pt/C at 10 mA cm^{-2} significantly increases after a short period, indicating a sharp decrease of activity. In contrast, SS Pt-RuO_2 HNSs||SS Pt-RuO_2 HNSs shows excellent stability with a small cell voltage increase within 100 hours (table S3). Note that SS Pt-RuO_2 HNSs||SS Pt-RuO_2 HNSs exhibit superior stability to the reported catalysts for overall water splitting in acidic media (Fig. 3D). Furthermore, the morphology and structure of SS Pt-RuO_2 HNSs are largely maintained after water splitting for 100-hour continuous operation (figs. S23 and S24). In sharp contrast, severe Pt agglomeration was observed for commercial Pt/C (note that commercial RuO_2/C generally suffers from poor stability for OER because of Ru dissolution in acidic conditions; fig. S25). In addition, we used SS Pt-RuO_2 HNSs as both cathode and anode catalysts in PEM electrolyzer in pure water to mimic the industrial water splitting operating systems. As shown in Fig. 3E, the chronopotentiometry tests of SS Pt-RuO_2 HNSs||SS Pt-RuO_2 HNSs show high stability without significant cell voltage increase over 100 hours at the current density of 100 mA cm^{-2}, indicating the great potential of SS Pt-RuO_2 HNSs for practical applications (Fig. 3F). In sharp contrast, commercial IrO_2||commercial Pt/C displays obviously inferior stability even in 4 hours at the same conditions (fig. S26).

Mechanism studies

In view of the excellent acidic water splitting activity, the electronic structure of SS Pt-RuO_2 HNSs was investigated by x-ray absorption spectroscopy measurement. The x-ray absorption near-edge structure (XANES) spectra at Pt L_3-edge indicate that Pt species are presented as oxidation state in the SS Pt-RuO_2 HNSs (Fig. 4A). The Fourier transforms of Pt L_3-edge extended x-ray absorption fine structure (EXAFS) spectra reveal that the Pt-O interatomic distance of SS Pt-RuO_2 HNSs is ~1.68 Å, which is larger than that of PtO_2 (Fig. 4B) (*35*). The absence of Pt-Pt coordination in the EXAFS spectrum of SS Pt-RuO_2 HNSs implies that Pt atoms present as isolated state. On the basis of the EXAFS spectra of Se mesh and SeO_2, we can conclude that Se species present as oxidation state in SS Pt-RuO_2 HNSs (Fig. 4C). For Ru, the *K*-edge XANES spectrum of SS Pt-RuO_2 HNSs displays similar features to those of RuO_2, indicating that Ru species in SS Pt-RuO_2 HNSs are in oxidation state. The intensity of the while line for the *K*-edge XANES spectrum of SS Pt-RuO_2 HNSs is slightly higher than that of RuO_2, suggesting the existence of electron transfer between Pt and RuO_2 (Fig. 4D), which is further validated by x-ray photoelectron spectroscopy (XPS) measurement (fig. S27). Compared to RuO_2, the interatomic distance of Ru-O bond in SS Pt-RuO_2 HNSs is expanded, which might be attributed to the formation of C-O bonds with the assistance of interstitial C (Fig. 4E) (*36*). Compared to commercial RuO_2/C, the strengthened intensity for C-O and positive shift of the binding energy in the C 1s XPS spectrum of SS Pt-RuO_2 HNSs suggest a much stronger interaction (fig. S27D). Moreover, the intensity of Ru-O bonds of SS Pt-RuO_2 HNSs is slightly weaker than that of RuO_2, indicating that the coordination environment of Ru is unsaturated, which may be attributed to the formation of oxygen vacancies (O_V) after Se evaporation (*37*–*39*). The formation of O_V in SS Pt-RuO_2 HNSs is further confirmed by O 1s XPS result (fig. S27E). To further study the local structure of O in SS Pt-RuO_2 HNSs, the O *K*-edge XANES spectra were collected. As shown in Fig. 4F, two sharp characteristic peaks at 528.7 and 531.9 eV, which are caused by the influence of crystal field, are assigned to the excitation of O 1s core electrons into hybridized states between O 2p and Ru 4d t_{2g} and e_g states (*40*), while the broad peak at 542.2 eV is attributed to the hybridization of the O 2p orbital with Ru 5sp states (*41*). The wavelet transform analysis further confirms results from EXAFS measurement (Fig. 4, G and H, and fig. S28). On the basis of the above results, the crystal structure of SS Pt-RuO_2 HNSs are provided, in

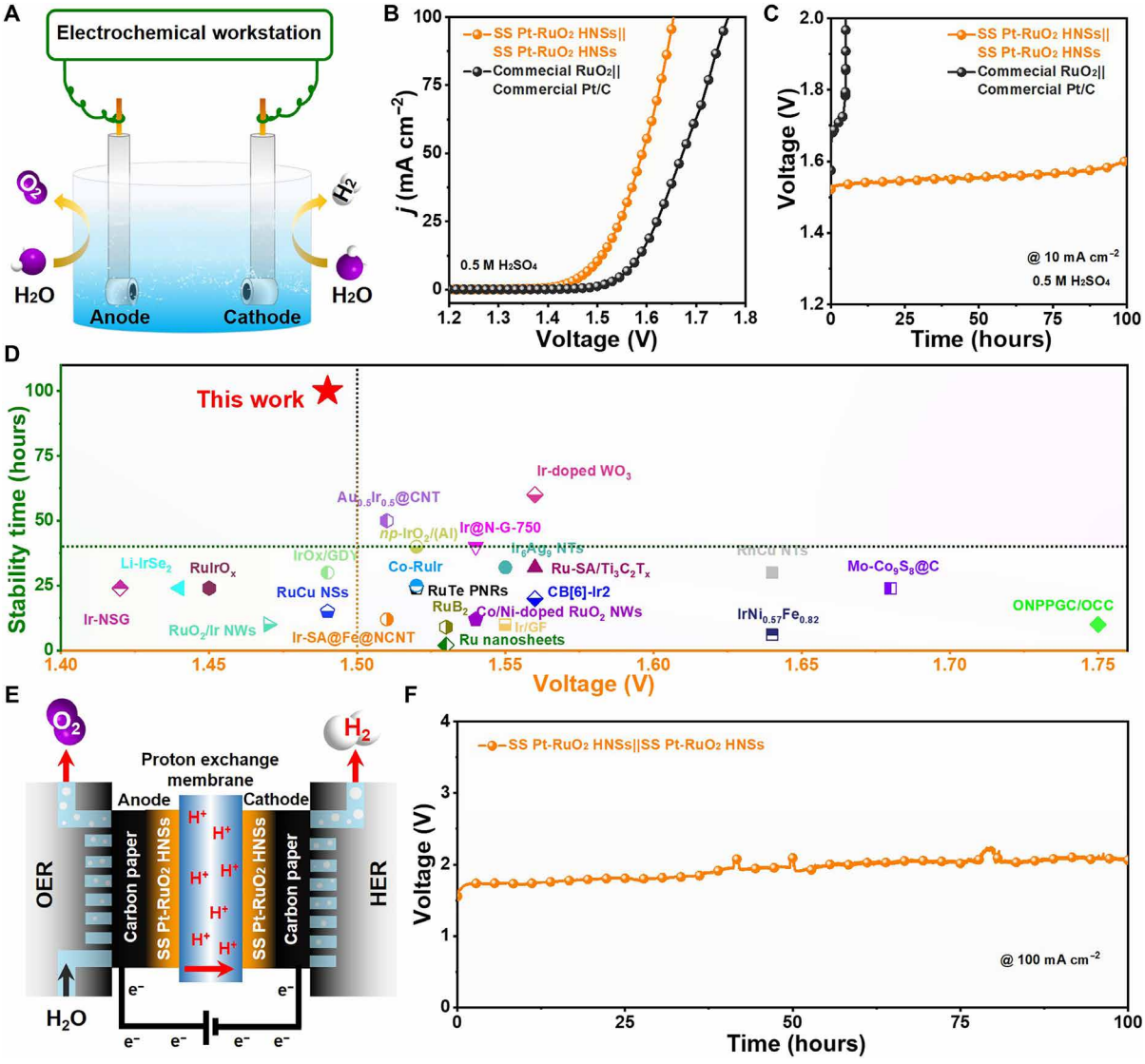

Fig. 3. Catalytic performance of overall water splitting. (**A**) Scheme of the two-electrode cell electrolyzer using SS Pt-RuO_2 HNSs as both the anode and cathode catalyst. (**B**) Polarization curves of SS Pt-RuO_2 HNSs||SS Pt-RuO_2 HNSs and commercial RuO_2||Pt/C in 0.5 M H_2SO_4 for water splitting. (**C**) Chronopotentiometry tests of SS Pt-RuO_2 HNSs||SS Pt-RuO_2 HNSs and commercial RuO_2||Pt/C at 10 mA cm^{-2}. (**D**) Comparison of the voltage and stability between SS Pt-RuO_2 HNSs and other reported catalysts for water splitting in acidic media. (**E**) Schematic diagram of the PEM electrolyzer. (**F**) Chronopotentiometry tests of SS Pt-RuO_2 HNSs||SS Pt-RuO_2 HNSs at 100 mA cm^{-2} in the PEM electrolyzer.

which Ru and O atoms are alternatively arrayed to form octahedral structure with Ru at the center and O at the vertex, while partial Ru atoms are replaced by Pt or Se atoms (Fig. 4I). In addition, C atoms insert into the gap to form interstitial atoms, and the existing interstitial C elongates the Ru-O and Pt-O bonds. Consequently, the strong interactions between SS Pt and RuO_2 significantly vary the electronic properties of catalysts and then improve the catalytic performance.

DFT calculations were performed to deepen the insight of enhanced OER performance on SS Pt-RuO_2 HNSs. Because of strongly oxidative conditions and corrosive electrolytes during operation, the catalyst stability in acidic electrolytes thus plays an important role in electrocatalysis (*42*). Theoretically, the dissociation energy for lattice O directly coordinated to the Ru core is a critical factor for the modeled RuO_2 system in determining the catalyst stability under acidic conditions (*43*). As shown in Fig. 5A, the dissociation energy of *O (i.e., ΔG_O) on SS Pt-RuO_2 HNSs is 1.22 eV higher than that on pure RuO_2, indicating the lattice O atom in SS Pt-RuO_2 HNSs is much more difficult to dissociate in the electrolyte solution. This will be effectively beneficial to enhance the stability of RuO_2 during electrocatalysis. Moreover, the superior reaction activity for SS Pt-RuO_2 HNSs to that of pure RuO_2 can be understood by using the energy change of potential determining step (PDS), that is, the formation of *OOH during OER reaction (*44*). As shown in Fig. 5B, the calculated ΔG for PDS on RuO_2 and SS Pt-RuO_2 HNSs are 2.02 and 1.738 eV, respectively, indicating that the doping of isolated Pt atoms can reduce energy barriers for OER, being consistent with the experimental observations. To deeply understand the origin of the enhanced OER activity for Pt-RuO_2, the Bader charge analysis

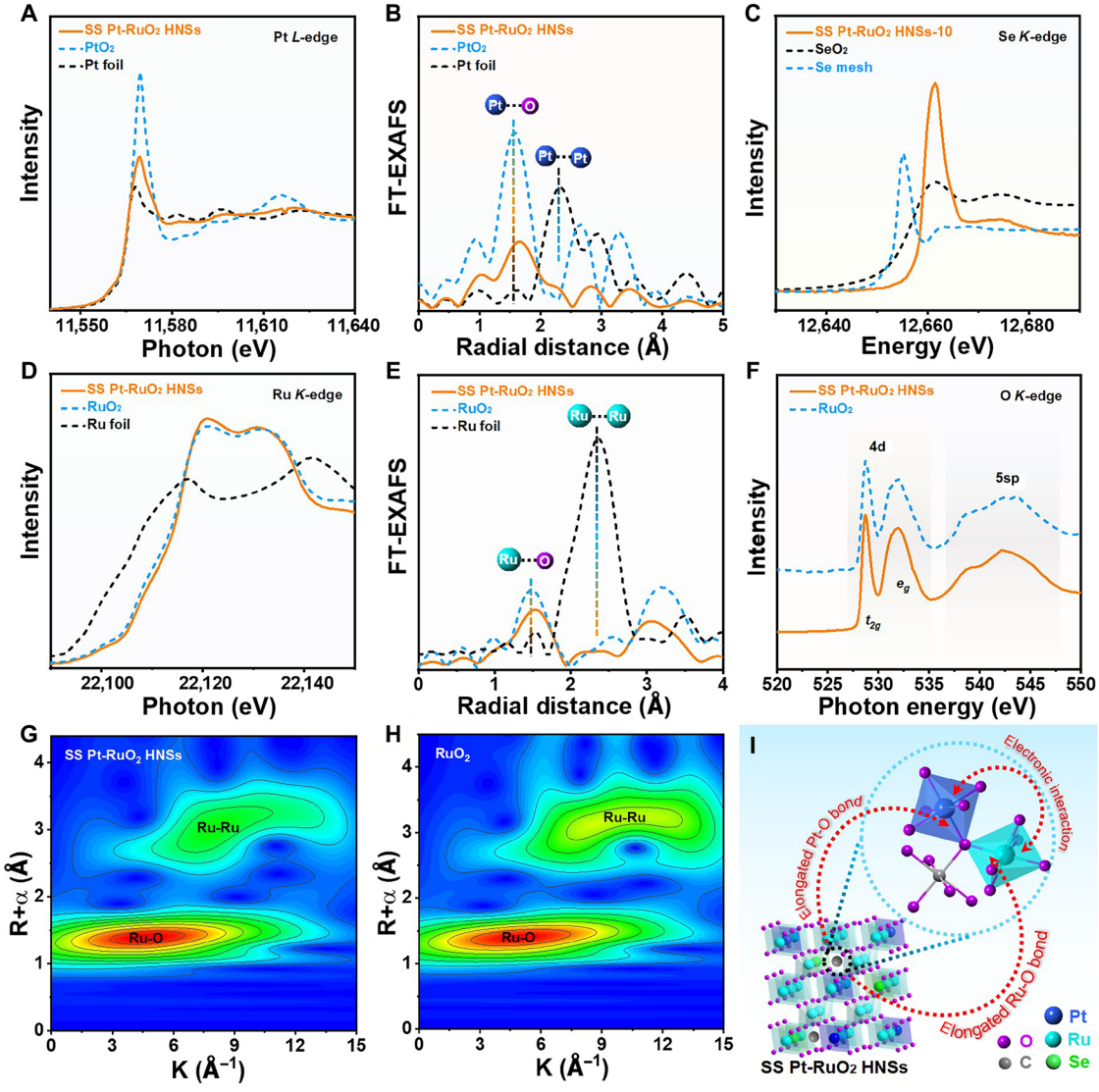

Fig. 4. Structural analysis of the catalysts. (**A**) Pt L_3-edge XANES and (**B**) Pt L_3-edge EXAFS spectra of SS Pt-RuO_2 HNSs, PtO_2, and Pt foil. (**C**) Se *K*-edge XANES spectra of SS Pt-RuO_2 HNSs, SeO_2, and Se mesh. (**D**) Ru *K*-edge XANES and (**E**) Ru *K*-edge EXAFS spectra of SS Pt-RuO_2 HNSs, commercial RuO_2, and Ru foil. (**F**) O *K*-edge XANES spectra of SS Pt-RuO_2 HNSs and commercial RuO_2. Wavelet transform of Ru *K*-edge EXAFS data of (**G**) SS Pt-RuO_2 HNSs and (**H**) commercial RuO_2. (**I**) Structural illustration of SS Pt-RuO_2 HNSs.

for pure RuO_2 and RuO_2 decorated with Pt single atom (Pt-RuO_2) were performed. We defined the SD (σ) of the charge numbers of O atoms as the descriptor to quantify the asymmetry degree. We found that the σ value in Pt-RuO_2 increases to 0.20 after loading Pt single atom, which is much larger than that of pure RuO_2 (0.16), indicating that the charge redistribution and charge density difference are attributed to the introduction of Pt single atom (Fig. 5C and fig. S29A). Moreover, the different electronic distribution will further affect the density of states (DOS). Hence, the Projected density of states (PDOS) for surface-active Ru atoms in pure RuO_2 and Pt-RuO_2 were calculated. As shown in Fig. 5D and fig. S29B, the 4d orbitals of active Ru atoms in Pt-RuO_2 are much closer to Fermi level than pure RuO_2, leading to the improved OER activity. On the basis of experimental and computational analysis, a possible acidic OER mechanism is proposed in Fig. 5E. At the beginning, water molecules will be readily adsorbed on the surface of SS Pt-RuO_2 HNSs. Hydrogen will be removed, and the electrons will be simultaneously generated to form M-O* species. With the participation of water molecules, M-O* will further evolve into M-OOH* and then to form O_2 after electron generation and dehydrogenation.

DISCUSSION

In summary, an ultrastable acidic water splitting electrocatalyst has been successfully created by doping SS Pt into RuO_2. The SS Pt-RuO_2 HNSs not only exhibit excellent OER and HER activity and stability but also show promising acidic water splitting performance in 0.5 M H_2SO_4. The required cell voltages of SS Pt-RuO_2 HNSs are 1.49, 1.59, and 1.65 V for reaching current densities of 10, 50, and 100 mA cm^{-2}, respectively, and their catalytic performance have

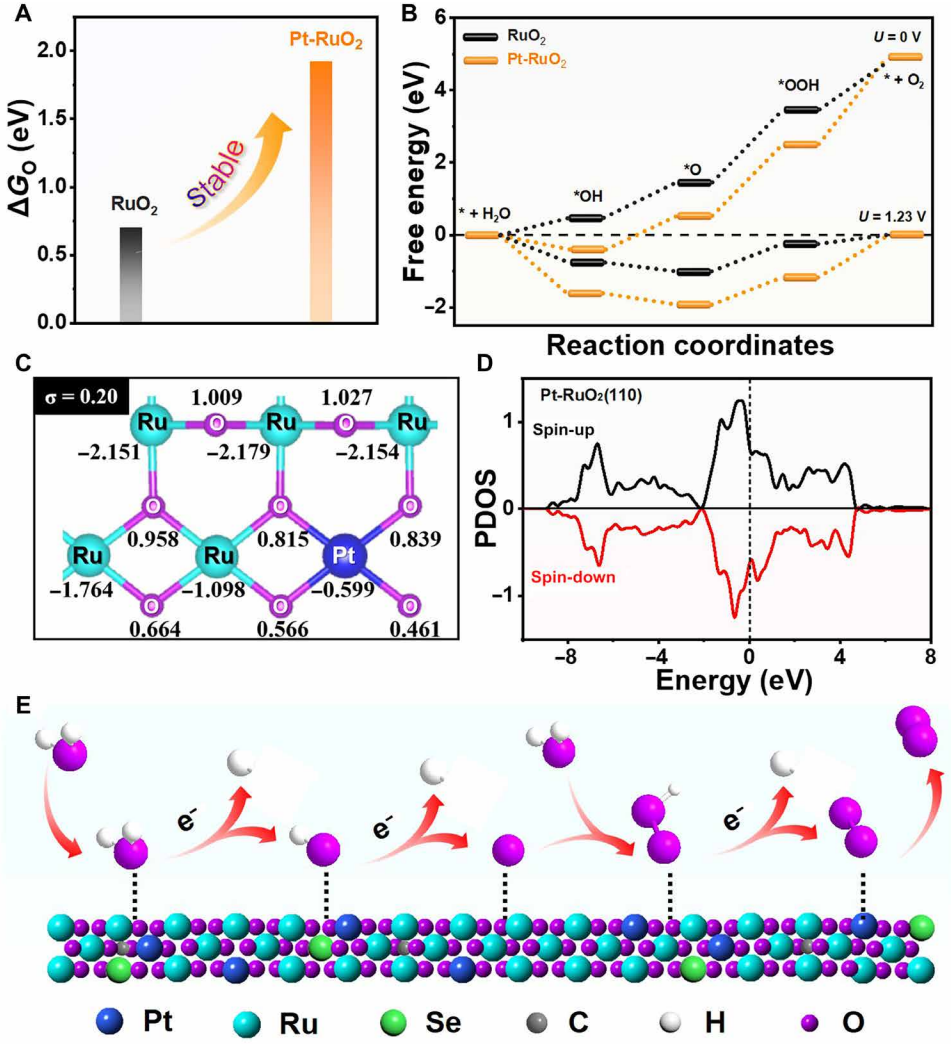

Fig. 5. DFT calculations. (**A**) The calculated dissociation energy of *O in RuO_2 and Pt-RuO_2, respectively. (**B**) The free energy profiles of OER process on RuO_2 and SS Pt-RuO_2 HNSs under the applied overpotential of 0 and 1.23 V (RHE), respectively. (**C**) The Bader charge numbers of atoms in Pt-RuO_2. Note that the negative value is referred to lose electrons, while the positive value mains to obtain electrons. (**D**) The PDOS of 4d orbitals of surface Ru atoms in Pt-RuO_2. (**E**) Schematic illustration of the mechanism for acidic OER on SS Pt-RuO_2 HNSs.

surpassed most reported catalysts. The SS Pt-RuO_2 HNSs exhibit excellent stability in 100 hours of continuous operation at 10 mA cm^{-2} and 100 hours in PEM electrolyzer at the current density of 100 mA cm^{-2}. Detailed experiments reveal that the presence of interstitial C can elongate the Ru-O and Pt-O bonds, and the introduced SS Pt significantly influences the electronic interaction of RuO_2. Theoretical calculations indicate that the strong synergy readily improves the OER activity by reducing the energy barriers and enhancing the dissociation energy of *O species. This work not only may provide a facile strategy for the modification of RuO_2 by doping SS Pt but also sheds new light on the practical application of overall water splitting.

MATERIALS AND METHODS

Chemicals

Hexaammineruthenium (III) chloride ($Cl_3H_{18}N_6Ru$, Ru 32.1%) was purchased from Alfa Aesar. Tetraammineplatinum (II) nitrate ($H_{12}N_6O_6Pt$, Pt 50%) was purchased from Beijing Hwrk Chemical Co. Ltd. Selenious acid (H_2SeO_3, 98%) was purchased from Sigma-Aldrich. Hydrazine hydrate aqueous solution ($N_2H_4{\cdot}H_2O$, AR) and isopropanol (IPA; AR) were purchased from Sinopharm Chemical Reagent Co. Ltd. Poly(vinylpyrrolidone) (PVP; average molecular weight 58,000, K15-19) was purchased from J&K Scientific Ltd.

Preparation of PtRuSe HNSs

For the preparation of PtRuSe HNSs, 7.7 mg of $Cl_3H_{18}N_6Ru$, 6.5 mg of H_2SeO_3, 0.5 mg of $H_{12}N_6O_6Pt$, and 50.0 mg of PVP were added into a mixture solution containing 10.0 ml of H_2O and 0.12 ml of N_2H_4 with ultrasonic treatment for 20 min. Then, the mixture solution was transferred into Teflon-sealed autoclave and heated at 180°C for 12 hours. Subsequently, the mixed solution was centrifuged and washed with ethanol/acetone.

Preparation of SS Pt-RuO_2 HNSs

The PtRuSe HNSs were added into a suspension consisting of carbon powders (VC-X72) and ethanol, and then, the above suspension

was sonicated for 30 min. Subsequently, the carbon-supported PtRuSe HNSs were centrifuged and dried at 60°C in a vacuum oven. Last, the carbon-supported PtRuSe HNSs were placed in a tube furnace and annealed at 300°C in air for 10 hours to obtain SS Pt-RuO_2 HNSs. Other PtRuSe HNSs synthesized by controlling the amount of $H_{12}N_6O_6Pt$ were selected for the preparation of pure RuO_2 HNSs, 2% Pt-RuO_2 HNSs, and 10% Pt-RuO_2 HNSs, respectively.

Characterizations

A Hitachi HT7700 TEM with an accelerating voltage of 120 kV was used to conduct low-magnification TEM analysis. The atomic structures of the SS Pt-RuO_2 HNSs images were taken on JEM-ARM200F with a cold-field emission gun and a spherical aberration corrector. HAADF-STEMs were conducted on a FEI Tecnai F20 TEM with an acceleration voltage of 200 kV. XRD analysis was carried out on X'Pert-Pro MPD diffractometer (PANalytical, Netherlands) with Cu Kα radiation. Raman spectra were carried out on a Raman spectrometer (LabRam HR 800) using 633-nm laser.

Electrochemical measurements

All the electrochemical tests were carried out on CHI660 workstation (CHI Instruments Inc., Shanghai) in 0.5 M H_2SO_4. HER and OER measurements were conducted with a standard three-electrode system. The overall water splitting measurements were carried out with a two-electrode setup. The ink was prepared by dispersing the catalyst to be tested homogeneously into the solution including 195 μl of IPA and 5 μl of Nafion (5%), followed by sonication for 30 min. The work electrode was prepared by dropping the ink (loading amount about 60 μg_{Ru}) onto the surface of the glassy carbon electrode (diameter, 5 mm). Graphite rod and saturated calomel electrode are used as counter and reference electrode, respectively. All polarization curves are the average of the stable polarization curves scanned in three experiments with 95% iR compensation.

DFT calculations

The quantum mechanics calculations were carried out using the VASP software at the version of 5.4.4, with the Perdew, Burke, and Ernzerhof flavor of DFT (*45*). The projector augmented wave method was used to account for core-valence interactions (*46*–*48*). The kinetic energy cutoff for plane wave expansions was set to 400 eV, and reciprocal space was sampled by the gamma-centered *k*-mesh with a grid of 3 × 3 × 1. The vacuum layer is at least 15 Å in the *z* direction to minimize possible interactions between the replicated cells. The convergence criteria are 1×10^{-5} eV energy differences for solving the electronic wave function. The Methfessel-Paxton smearing of second order with a width of 0.1 eV was applied. All geometries (atomic coordinates) were converged to within 1×10^{-2} eV $Å^{-1}$ for maximal components of forces. A post-stage Van der Waals DFT-D3 method with Becke-Johnson damping was applied (*49*).

Our simulation model was taken from the experimental RuO_2 structure with lattice parameters of $a = b = 4.54$ Å, $c = 3.13$ Å, respectively. For pure RuO_2, A 3 × 3 × 4 RuO_2 (110) surface slab model was constructed, with the bottom two layers fixed and the top two layers relaxed. Note that the (110) surface has two kinds of Ru site; one site is saturated with six oxygen atoms, and another site was cooperated with five oxygen atoms, which is the active site. For SS Pt-RuO_2 HNSs, one surface Ru atom near the active site was replaced by Pt to mimic the experimental observed structure.

Adsorption behavior of *O, *OH, and *OOH intermediates for each catalyst and each model was optimized to convergence. The Δ*G* for each OER step was calculated through the model of computational hydrogen electrode along with the equation as follows

$$\Delta G = \Delta E_{\mathrm{DFT}} + \Delta \mathrm{ZPE} - T\Delta S$$

where ΔE_{DFT}, ΔZPE, Δ*S*, and *T* are the changes in DFT total energy, zero-point energy, entropy from the initial state to the final state, and temperature, respectively. ΔZPE and Δ*S* can be obtained by the NIST-JANAF thermodynamics table for gaseous molecules and by calculating the vibrational frequencies for the reactive intermediates, respectively (*50*). The entropy of the chemisorbed intermediates only takes the vibrational entropy into account. The formula for calculating the dissociation energy of *O (ΔG_O) is given as follows

$$\Delta G_{\mathrm{O}} = G_{\mathrm{sur}} + (G_{\mathrm{H2O}} - G_{\mathrm{H2}}) - G(*_{\mathrm{O}})$$

where G_{sur}, $G(*_O)$ G_{H2O}, and G_{H2} represent the surface energy without absorbate, the energy that adsorbs the structure of *O intermediate, the energy for water molecules, and the energy for hydrogen molecules, respectively.

SUPPLEMENTARY MATERIALS

Supplementary material for this article is available at https://science.org/doi/10.1126/sciadv.abl9271

REFERENCES AND NOTES

1. L. Li, P. Wang, Q. Shao, X. Huang, Metallic nanostructures with low dimensionality for electrochemical water splitting. *Chem. Soc. Rev.* **49**, 3072–3106 (2020).
2. Y. Zhou, S. Sun, C. Wei, Y. Sun, P. Xi, Z. Feng, Z. J. Xu, Significance of engineering the octahedral units to promote the oxygen evolution reaction of spinel oxides. *Adv. Mater.* **31**, 1902509 (2019).
3. C. Wei, S. Sun, D. Mandler, X. Wang, S. Z. Qiao, Z. J. Xu, Approaches for measuring the surface areas of metal oxide electrocatalysts for determining their intrinsic electrocatalytic activity. *Chem. Soc. Rev.* **48**, 2518–2534 (2019).
4. Z. Xiao, Y. C. Huang, C. L. Dong, C. Xie, Z. Liu, S. Du, W. Chen, D. Yan, L. Tao, Z. Shu, G. Zhang, H. Duan, Y. Wang, Y. Zou, R. Chen, S. Wang, Operando identification of the dynamic behavior of oxygen vacancy-rich Co_3O_4 for oxygen evolution reaction. *J. Am. Chem. Soc.* **142**, 12087–12095 (2020).
5. Z. Liu, G. Wang, X. Zhu, Y. Wang, Y. Zou, S. Zang, S. Wang, Optimal geometrical configuration of cobalt cations in spinel oxides to promote oxygen evolution reaction. *Angew. Chem. Int. Ed.* **59**, 4736–4742 (2020).
6. M. Li, K. Duanmu, C. Wan, T. Cheng, L. Zhang, S. Dai, W. Chen, Z. Zhao, P. Li, H. Fei, Y. Zhu, R. Yu, J. Luo, K. Zang, Z. Lin, M. Ding, J. Huang, H. Sun, J. Guo, X. Pan, W. A. Goddard III, P. Sautet, Y. Huang, X. Duan, Single-atom tailoring of platinum nanocatalysts for high-performance multifunctional electrocatalysis. *Nat. Catal.* **2**, 495–503 (2019).
7. L. An, J. Feng, Y. Zhang, R. Wang, H. Liu, G. C. Wang, F. Cheng, P. Xi, Epitaxial heterogeneous interfaces on N-$NiMoO_4$/NiS_2 nanowires/nanosheets to boost hydrogen and oxygen production for overall water splitting. *Adv. Funct. Mater.* **29**, 1805298 (2019).
8. J. X. Feng, H. Xu, S. H. Ye, G. Ouyang, Y. X. Tong, G. R. Li, Silica-polypyrrole hybrids as high-performance metal-free electrocatalysts for the hydrogen evolution reaction in neutral media. *Angew. Chem. Int. Ed.* **56**, 8120–8124 (2017).
9. R. Li, H. Wang, F. Hu, K. C. Chan, X. Liu, Z. Lu, J. Wang, Z. Li, L. Zeng, Y. Li, X. Wu, Y. Xiong, IrW nanochannel support enabling ultrastable electrocatalytic oxygen evolution at 2 A cm^{-2} in acidic media. *Nat. Commun.* **12**, 3540 (2021).
10. A. Ali, P. K. Shen, Recent progress in graphene-based nanostructured electrocatalysts for overall water splitting. *Electrochem. Energy Rev.* **3**, 370–394 (2020).
11. D. Zhao, Z. Zhuang, X. Cao, C. Zhang, Q. Peng, C. Chen, Y. Li, Atomic site electrocatalysts for water splitting, oxygen reduction and selective oxidation. *Chem. Soc. Rev.* **49**, 2215–2264 (2020).
12. Q. Wang, C.-Q. Xu, W. Liu, S.-F. Hung, H. B. Yang, J. Gao, W. Cai, H. M. Chen, J. Li, B. Liu, Coordination engineering of iridium nanocluster bifunctional electrocatalyst for highly efficient and pH-universal overall water splitting. *Nat. Commun.* **11**, 4246 (2020).

13. J. Wang, L. Han, B. Huang, Q. Shao, H. L. Xin, X. Huang, Amorphization activated ruthenium-tellurium nanorods for efficient water splitting. *Nat. Commun.* **10**, 5692 (2019).
14. D. Chen, T. Liu, P. Wang, J. Zhao, C. Zhang, R. Cheng, W. Li, P. Ji, Z. Pu, S. Mu, Ionothermal route to phase-pure RuB_2 catalysts for efficient oxygen evolution and water splitting in acidic media. *ACS Energy Lett.* **5**, 2909–2915 (2020).
15. C. Shang, C. Cao, D. Yu, Y. Yan, Y. Lin, H. Li, T. Zheng, X. Yan, W. Yu, S. Zhou, J. Zeng, Electron correlations engineer catalytic activity of pyrochlore iridates for acidic water oxidation. *Adv. Mater.* **31**, 1805104 (2019).
16. T. Zheng, C. Shang, Z. He, X. Wang, C. Cao, H. Li, R. Si, B. Pan, S. Zhou, J. Zeng, Intercalated iridium diselenide electrocatalysts for efficient pH-universal water splitting. *Angew. Chem. Int. Ed.* **58**, 14764–14769 (2019).
17. J. Li, Y. Wang, T. Zhou, H. Zhang, X. Sun, J. Tang, L. Zhang, A. M. Al-Enizi, Z. Yang, G. Zheng, Nanoparticle superlattices as efficient bifunctional electrocatalysts for water splitting. *J. Am. Chem. Soc.* **137**, 14305–14312 (2015).
18. X. Li, L. Zhao, J. Yu, X. Liu, X. Zhang, H. Liu, W. Zhou, Water splitting: From electrode to green energy system. *Nanomicro Lett.* **12**, 131 (2020).
19. W. Gao, Z. Xia, F. Cao, J. C. Ho, Z. Jiang, Y. Qu, Comprehensive understanding of the spatial configurations of CeO_2 in NiO for the electrocatalytic oxygen evolution reaction: Embedded or surface-loaded. *Adv. Funct. Mater.* **28**, 1706065 (2018).
20. D. Chen, M. Qiao, Y. R. Lu, L. Hao, D. Liu, C. L. Dong, Y. Li, S. Wang, Preferential cation vacancies in perovskite hydroxide for the oxygen evolution reaction. *Angew. Chem. Int. Ed.* **57**, 8691–8696 (2018).
21. Q. Yao, B. Huang, N. Zhang, M. Sun, X. Huang, Channel rich RuCu nanosheets for pH-universal overall water splitting electrocatalysis. *Angew. Chem. Int. Ed.* **58**, 14121–14126 (2019).
22. J. Wang, Y. Ji, R. Yin, Y. Li, Q. Shao, X. Huang, Transition metal-doped ultrathin RuO_2 networked nanowires for efficient overall water splitting across a broad pH range. *J. Mater. Chem. A* **7**, 6411–6416 (2019).
23. G. Meng, W. Sun, A. A. Mon, X. Wu, L. Xia, A. Han, Y. Wang, Z. Zhuang, J. Liu, D. Wang, Y. Li, Strain regulation to optimize the acidic water oxidation performance of atomic-layer IrO_x. *Adv. Mater.* **31**, 1903616 (2019).
24. J. Gao, C. Q. Xu, S. F. Hung, W. Liu, W. Cai, Z. Zeng, C. Jia, H. M. Chen, H. Xiao, J. Li, Y. Huang, B. Liu, Breaking long-range order in iridium oxide by alkali ion for efficient water oxidation. *J. Am. Chem. Soc.* **141**, 3014–3023 (2019).
25. J. Liu, Y. Zheng, Y. Jiao, Z. Wang, Z. Lu, A. Vasileff, S. Z. Qiao, NiO as a bifunctional promoter for RuO_2 toward superior overall water splitting. *Small* **14**, 1704073 (2018).
26. A. Oh, Y. Kim, H. Baik, B. Kim, K. Chaudhari, S. H. Joo, K. Lee, Topotactic transformations in an icosahedral nanocrystal to form efficient water-splitting catalysts. *Adv. Mater.* **31**, 1805546 (2018).
27. Y. Yao, S. Hu, W. Chen, Z. Q. Huang, W. Wei, T. Yao, R. Liu, K. Zang, X. Wang, G. Wu, W. Yuan, T. Yuan, B. Zhu, W. Liu, Z. Li, D. He, Z. Xue, Y. Wang, X. Zheng, J. Dong, C. R. Chang, Y. Chen, X. Hong, J. Luo, S. Wei, W. X. Li, P. Strasser, Y. Wu, Y. Li, Engineering the electronic structure of single atom Ru sites via compressive strain boosts acidic water oxidation electrocatalysis. *Nat. Catal.* **2**, 304–313 (2019).
28. D. Wu, K. Kusada, S. Yoshioka, T. Yamamoto, T. Toriyama, S. Matsumura, Y. Chen, O. Seo, J. Kim, C. Song, S. Hiroi, O. Sakata, T. Ina, S. Kawaguchi, Y. Kubota, H. Kobayashi, H. Kitagawa, Efficient overall water splitting in acid with anisotropic metal nanosheets. *Nat. Commun.* **12**, 1145 (2021).
29. X. Cui, P. Ren, C. Ma, J. Zhao, R. Chen, S. Chen, N. P. Rajan, H. Li, L. Yu, Z. Tian, D. Deng, Robust interface Ru centers for high-performance acidic oxygen evolution. *Adv. Mater.* **32**, 1908126 (2020).
30. J. Sun, R. Ge, K. Jiang, Y. Dong, F. Hao, Z. Tian, G. Chen, L. Chen, Assembling ultrasmall copper-doped ruthenium oxide nanocrystals into hollow porous polyhedra: Highly robust electrocatalysts for oxygen evolution in acidic media. *Adv. Mater.* **30**, 1801351 (2018).
31. J. Shan, C. Guo, Y. Zhu, S. Chen, L. Song, M. Jaroniec, Y. Zheng, S. Z. Qiao, Charge-redistribution-enhanced nanocrystalline Ru@IrO_x electrocatalysts for oxygen evolution in acidic media. *Chem* **5**, 445–459 (2019).
32. Q. Jiang, N. Kurra, M. Alhabeb, Y. Gogotsi, H. Alshareef, All pseudocapacitive MXene-RuO_2 asymmetric supercapacitors. *Adv. Energy Mater.* **8**, 1703043 (2018).
33. X. Li, L. Liu, X. Ren, J. Gao, Y. Huang, B. Liu, All microenvironment modulation of single-atom catalysts and their roles in electrochemical energy conversion. *Sci. Adv.* **6**, eabb6833 (2020).
34. N. Cheng, L. Zhang, K. Doyle-Davis, X. Sun, Single-atom catalysts: From design to application. *Electrochem. Energy Rev.* **2**, 539–573 (2019).
35. Y. Zhu, X. Zhu, L. Bu, Q. Shao, Y. Li, Z. Hu, C. T. Chen, C. W. Pao, S. Yang, X. Huang, Single-atom in-doped subnanometer Pt nanowires for simultaneous hydrogen generation and biomass upgrading. *Adv. Funct. Mater.* **30**, 2004310 (2020).
36. Y. Lin, Z. Tian, L. Zhang, J. Ma, Z. Jiang, B. Deibert, R. Ge, L. Chen, Chromium-ruthenium oxide solid solution electrocatalyst for highly efficient oxygen evolution reaction in acidic media. *Nat. Commun.* **10**, 162 (2019).
37. X. Wang, L. Zhuang, Y. Jia, H. Liu, X. Yan, L. Zhang, D. Yang, Z. Zhu, X. Yao, Plasma-triggered synergy of exfoliation, phase transformation, and surface engineering in cobalt diselenide for enhanced water oxidation. *Angew. Chem. Int. Ed.* **57**, 16421–16425 (2018).
38. Z. Wu, Y. Zhao, W. Jin, B. Jia, J. Wang, T. Ma, Recent progress of vacancy engineering for electrochemical energy conversion related applications. *Adv. Funct. Mater.* **31**, 2009070 (2021).
39. X. Yan, Y. Jia, X. Yao, Defective structures in metal compounds for energy-related electrocatalysis. *Small Struct.* **2**, 2000067 (2021).
40. Z. Hu, H. Von Lips, M. S. Golden, J. Fink, G. Kaindl, F. M. F. de Groot, S. Ebbinghaus, A. Reller, Multiplet effects in the Ru $L_{2,3}$ x-ray-absorption spectra of Ru(IV) and Ru(V) compounds. *Phys. Rev. B* **61**, 5262–5266 (2000).
41. J. Zhou, J. Wang, H. Fang, C. Wu, J. N. Cutler, T. K. Sham, Nanoscale chemical imaging and spectroscopy of individual RuO_2 coated carbon nanotubes. *Chem. Commun.* **46**, 2778–2780 (2010).
42. H. Sun, Z. Yan, F. Liu, W. Xu, F. Cheng, J. Chen, Self-supported transition-metal-based electrocatalysts for hydrogen and oxygen evolution. *Adv. Mater.* **32**, 1806326 (2019).
43. S. Hao, M. Liu, J. Pan, X. Liu, X. Tan, N. Xu, Y. He, L. Lei, X. Zhang, Dopants fixation of ruthenium for boosting acidic oxygen evolution stability and activity. *Nat. Commun.* **11**, 5368 (2020).
44. V. Viswanathan, H. A. Hansen, J. Rossmeisl, J. K. Nørskov, Unifying the $2e^-$ and $4e^-$ reduction of oxygen on metal surfaces. *J. Phys. Chem. Lett.* **3**, 2948–2951 (2012).
45. G. Kresse, J. Furthmüller, Efficient iterative schemes for ab initio total-energy calculations using a plane-wave basis set. *Phys. Rev. B* **54**, 11169–11186 (1996).
46. J. P. Perdew, J. A. Chevary, S. H. Vosko, K. A. Jackson, M. R. Pederson, D. J. Singh, C. Fiolhais, Atoms, molecules, solids, and surfaces: Applications of the generalized gradient approximation for exchange and correlation. *Phys. Rev. B Condens. Matter* **46**, 6671–6687 (1992).
47. J. P. Perdew, J. A. Chevary, S. H. Vosko, K. A. Jackson, M. R. Pederson, D. J. Singh, C. Fiolhais, Erratum: Atoms, molecules, solids, and surfaces: Applications of the generalized gradient approximation for exchange and correlation. *Phys. Rev. B Condens. Matter* **48**, 4978 (1993).
48. S. Wang, E. Zhu, Y. Huang, H. Heinz, Direct correlation of oxygen adsorption on platinum-electrolyte interfaces with the activity in the oxygen reduction reaction. *Sci. Adv.* **7**, eabb1435 (2021).
49. S. Grimme, S. Ehrlich, L. Goerigk, Effect of the damping function in dispersion corrected density functional theory. *J. Comput. Chem.* **32**, 1456–1465 (2011).
50. W. Malcolm, J. R. Chase, *NIST-JANAF Thermochemical Tables* (American Institute of Physics, 1998).
51. L. C. Seitz, C. F. Dickens, K. Nishio, Y. Hikita, J. Montoya, A. Doyle, C. Kirk, A. Vojvodic, H. Y. Hwang, J. K. Norskov, T. F. Jaramillo, A highly active and stable $IrO_x/SrIrO_3$ catalyst for the oxygen evolution reaction. *Science* **353**, 1011–1014 (2016).
52. J. Chen, P. Cui, G. Zhao, K. Rui, M. Lao, Y. Chen, X. Zheng, Y. Jiang, H. Pan, S. X. Dou, W. Sun, Low-coordinate iridium oxide confined on graphitic carbon nitride for highly efficient oxygen evolution. *Angew. Chem. Int. Ed.* **58**, 12540–12544 (2019).
53. L. Yang, G. Yu, X. Ai, W. Yan, H. Duan, W. Chen, H. Duan, X. Li, T. Wang, C. Zhang, X. Huang, J. S. Chen, X. Zou, Efficient oxygen evolution electrocatalysis in acid by a perovskite with face-sharing IrO_6 octahedral dimers. *Nat. Commun.* **9**, 5236 (2018).
54. Y. Pi, J. Guo, Q. Shao, X. Huang, Highly efficient acidic oxygen evolution electrocatalysis enabled by porous Ir-Cu nanocrystals with three-dimensional electrocatalytic surfaces. *Chem. Mater.* **30**, 8571–8578 (2018).
55. X. Liang, L. Shi, Y. Liu, H. Chen, R. Si, W. Yan, Q. Zhang, G. D. Li, L. Yang, X. Zou, Activating inert, nonprecious perovskites with iridium dopants for efficient oxygen evolution reaction under acidic conditions. *Angew. Chem. Int. Ed.* **131**, 7713–7717 (2019).
56. D. Cao, H. Xu, D. Cheng, Construction of defect-Rich RhCu nanotubes with highly active Rh_3Cu_1 alloy phase for overall water splitting in all pH values. *Adv. Energy Mater.* **10**, 1903038 (2020).
57. F. Luo, H. Hu, X. Zhao, Z. Yang, Q. Zhang, J. Xu, T. Kaneko, Y. Yoshida, C. Zhu, W. Cai, Robust and stable acidic overall water splitting on Ir single atoms. *Nano Lett.* **20**, 2120–2128 (2020).
58. L. Zhang, H. Jang, H. Liu, M. G. Kim, D. Yang, S. Liu, X. Liu, J. Cho, Sodium-decorated amorphous/crystalline RuO_2 with rich oxygen vacancies: A robust pH-universal oxygen evolution electrocatalyst. *Angew. Chem. Int. Ed.* **60**, 18821–18829 (2021).
59. J. Yang, Y. Ji, Q. Shao, N. Zhang, Y. Li, X. Huang, A universal strategy to metal wavy nanowires for efficient electrochemical water splitting at pH-universal conditions. *Adv. Funct. Mater.* **28**, 1803722 (2018).
60. J. Xu, Z. Lian, B. Wei, Y. Li, O. Bondarchuk, N. Zhang, Z. Yu, A. Araujo, I. Amorim, Z. Wang, B. Li, L. Liu, Strong electronic coupling between ultrafine iridium–ruthenium nanoclusters and conductive, acid-stable tellurium nanoparticle support for efficient and durable oxygen evolution in acidic and neutral media. *ACS Catal.* **10**, 3571–3579 (2020).

61. S. Choi, J. Park, M. K. Kabiraz, Y. Hong, T. Kwon, T. Kim, A. Oh, H. Baik, M. Lee, S.-M. Peak, S.-I. Choi, K. Lee, Pt dopant: Controlling the Ir oxidation states toward efficient and durable oxygen evolution reaction in acidic media. *Adv. Funct. Mater.* **30**, 2003935 (2020).
62. J. Shan, T. Ling, K. Davey, Y. Zheng, S. Z. Qiao, Transition-metal-doped RuIr bifunctional nanocrystals for overall water splitting in acidic environments. *Adv. Mater.* **31**, 1900510 (2019).
63. H. Guo, Z. Fang, H. Li, D. Fernandez, G. Henkelman, S. M. Humphrey, G. Yu, Rational design of rhodium–iridium alloy nanoparticles as highly active catalysts for acidic oxygen evolution. *ACS Nano* **13**, 13225–13234 (2019).
64. Y. Pi, Y. Xu, L. Li, T. Sun, B. Huang, L. Bu, Y. Ma, Z. Hu, C. W. Pao, X. Huang, Selective surface reconstruction of a defective iridium-based catalyst for high-efficiency water splitting. *Adv. Funct. Mater.* **30**, 2004375 (2020).
65. L. Cao, Q. Luo, J. Chen, L. Wang, Y. Lin, H. Wang, X. Liu, X. Shen, W. Zhang, W. Liu, Z. Qi, Z. Jiang, J. Yang, T. Yao, Dynamic oxygen adsorption on single-atomic ruthenium catalyst with high performance for acidic oxygen evolution reaction. *Nat. Commun.* **10**, 4849 (2019).
66. S. Laha, Y. Lee, F. Podjaski, D. Weber, V. Duppel, L. M. Schoop, F. Pielhofer, C. Scheurer, K. Müller, U. Starke, K. Reuter, B. V. Lotsch, Ruthenium oxide nanosheets for enhanced oxygen evolution catalysis in acidic medium. *Adv. Energy Mater.* **9**, 1803795 (2019).
67. G. Wu, X. Zheng, P. Cui, H. Jiang, X. Wang, Y. Qu, W. Chen, Y. Lin, H. Li, X. Han, Y. Hu, P. Liu, Q. Zhang, J. Ge, Y. Yao, R. Sun, Y. Wu, L. Gu, X. Hong, Y. Li, A general synthesis approach for amorphous noble metal nanosheets. *Nat. Commun.* **10**, 4855 (2019).
68. C. Lei, H. Chen, J. Cao, J. Yang, M. Qiu, Y. Xia, C. Yuan, B. Yang, Z. Li, X. Zhang, L. Lei, J. Abbott, Y. Zhong, X. Xia, G. Wu, Q. He, Y. Hou, FeN_4 sites embedded into carbon nanofiber integrated with electrochemically exfoliated graphene for oxygen evolution in acidic medium. *Adv. Energy Mater.* **8**, 1801912 (2018).
69. X. Miao, L. Zhang, L. Wu, Z. Hu, L. Shi, S. Zhou, Quadruple perovskite ruthenate as a highly efficient catalyst for acidic water oxidation. *Nat. Commun.* **10**, 3809 (2019).
70. D. Liu, X. Li, S. Chen, H. Yan, C. Wang, C. Wu, Y. A. Haleem, S. Duan, J. Lu, B. Ge, P. M. Ajayan, Y. Luo, J. Jiang, L. Song, Atomically dispersed platinum supported on curved carbon supports for efficient electrocatalytic hydrogen evolution. *Nat. Energy* **4**, 512–518 (2019).
71. M. Liu, J. A. Wang, W. Klysubun, G. G. Wang, S. Sattayaporn, F. Li, Y. W. Cai, F. Zhang, J. Yu, Y. Yang, Interfacial electronic structure engineering on molybdenum sulfide for robust dual-pH hydrogen evolution. *Nat. Commun.* **12**, 5260 (2021).
72. X. Huang, X. Xu, C. Li, D. Wu, D. Cheng, D. Cao, Vertical CoP nanoarray wrapped by N, P-doped carbon for hydrogen evolution reaction in both acidic and alkaline conditions. *Adv. Energy Mater.* **9**, 1803970 (2019).
73. K. Khan, T. Liu, M. Arif, X. Yan, M. D. Hossain, F. Rehman, S. Zhou, J. Yang, C. Sun, S. H. Bae, J. Kim, K. Amine, X. Pan, Z. Luo, Laser-irradiated holey graphene-supported single-atom catalyst towards hydrogen evolution and oxygen reduction. *Adv. Energy Mater.* **11**, 21001619 (2021).
74. W. Gao, M. Yan, H. Y. Cheung, Z. Xia, X. Zhou, Y. Qin, C. Y. Wong, J. C. Ho, C. R. Chang, Y. Qu, Modulating electronic structure of CoP electrocatalysts towards enhanced hydrogen evolution by Ce chemical doping in both acidic and basic media. *Nano Energy* **38**, 290–296 (2017).
75. Z. J. Wang, M. X. Li, J. H. Yu, X. B. Ge, Y. H. Liu, W. H. Wang, Low-iridium-content IrNiTa metallic glass films as intrinsically active catalysts for hydrogen evolution reaction. *Adv. Mater.* **32**, 1906384 (2020).
76. M. Zhu, Q. Shao, Y. Qian, X. Huang, Superior overall water splitting electrocatalysis in acidic conditions enabled by bimetallic Ir-Ag nanotubes. *Nano Energy* **56**, 330–337 (2019).
77. M. Kim, M. A. R. Anjum, M. Lee, B. J. Lee, J. S. Lee, Activating MoS_2 basal plane with Ni_2P nanoparticles for Pt-like hydrogen evolution reaction in acidic media. *Adv. Funct. Mater.* **29**, 1809151 (2019).
78. Y. Pi, Q. Shao, P. Wang, J. Guo, X. Huang, General formation of monodisperse IrM (M = Ni, Co, Fe) bimetallic nanoclusters as bifunctional electrocatalysts for acidic overall water splitting. *Adv. Funct. Mater.* **27**, 1700886 (2017).
79. L. Zhang, Y. Jia, G. Gao, X. Yan, N. Chen, J. Chen, M. T. Soo, B. Wood, D. Yang, A. Du, X. Yao, Graphene defects trap atomic Ni species for hydrogen and oxygen evolution reactions. *Chem* **4**, 285–297 (2018).
80. Z. Pu, I. S. Amiinu, Z. Kou, W. Li, S. Mu, RuP_2-based catalysts with platinum-like activity and higher durability for the hydrogen evolution reaction at all pH values. *Angew. Chem. Int. Ed.* **56**, 11559–11564 (2017).
81. W. Chen, J. Pei, C.-T. He, J. Wan, H. Ren, Y. Wang, J. Dong, K. Wu, W.-C. Cheong, J. Mao, X. Zheng, W. Yan, Z. Zhuang, C. Chen, Q. Peng, D. Wang, Y. Li, Single tungsten atoms supported on MOF-derived N-doped carbon for robust electrochemical hydrogen evolution. *Adv. Mater.* **30**, 1800396 (2018).
82. H. Wei, Q. Xi, X. Chen, D. Guo, F. Ding, Z. Yang, S. Wang, J. Li, S. Huang, Molybdenum carbide nanoparticles coated into the graphene wrapping N-doped porous carbon microspheres for highly efficient electrocatalytic hydrogen evolution both in acidic and alkaline media. *Adv. Sci.* **5**, 1700733 (2018).
83. C. Yang, R. Zhao, H. Xiang, J. Wu, W. Zhong, W. Li, Q. Zhang, N. Yang, X. Li, Ni-activated transition metal carbides for efficient hydrogen evolution in acidic and alkaline solutions. *Adv. Energy Mater.* **10**, 2002260 (2020).
84. C. Zhang, Y. Cui, Y. Yang, L. Lu, S. Yu, Z. Meng, Y. Wu, Y. Li, Y. Wang, H. Tian, W. Zheng, Highly conductive amorphous pentlandite anchored with ultrafine platinum nanoparticles for efficient pH-universal hydrogen evolution reaction. *Adv. Funct. Mater.* **27**, 2105372 (2021).
85. D. H. Kweon, M. S. Okyay, S.-J. Kim, J.-P. Jeon, H.-J. Noh, N. Park, J. Mahmood, J.-B. Baek, Ruthenium anchored on carbon nanotube electrocatalyst for hydrogen production with enhanced Faradaic efficiency. *Nat. Commun.* **11**, 1278 (2021).
86. S. L. Zhang, X. F. Lu, Z.-P. Wu, D. Luan, X. W. Lou, Engineering platinum–cobalt nano-alloys in porous nitrogen-doped carbon nanotubes for highly efficient electrocatalytic hydrogen evolution. *Angew. Chem. Int. Ed.* **60**, 19068–19073 (2021).
87. Y. Liu, S. Liu, Y. Wang, Q. Zhang, L. Gu, S. Zhao, D. Xu, Y. Li, J. Bao, Z. Dai, Ru modulation effects in the synthesis of unique rod-like Ni@Ni_2P–Ru heterostructures and their remarkable electrocatalytic hydrogen evolution performance. *J. Am. Chem. Soc.* **140**, 2731–2734 (2018).
88. X. Xiao, H. Zhang, Y. Xiong, F. Liang, Y. W. Yang, Iridium-doped N-rich mesoporous carbon electrocatalyst with synthetic macrocycles as carbon source for hydrogen evolution reaction. *Adv. Funct. Mater.* **31**, 2105562 (2021).
89. X. Wu, B. Feng, W. Li, Y. Niu, Y. Yu, S. Lu, C. Zhong, P. Liu, Z. Tian, L. Chen, W. Hu, C. M. Li, Metal-support interaction boosted electrocatalysis of ultrasmall iridium nanoparticles supported on nitrogen doped graphene for highly efficient water electrolysis in acidic and alkaline media. *Nano Energy* **62**, 117–126 (2019).
90. X. Peng, S. Zhao, Y. Mi, L. Han, X. Liu, D. Qi, J. Sun, Y. Liu, H. Bao, L. Zhuo, H. L. Xin, J. Luo, X. Sun, Trifunctional single-atomic Ru sites enable efficient overall water splitting and oxygen reduction in acidic media. *Small* **16**, 2002888 (2020).
91. X. Zhang, Z. Luo, P. Yu, Y. Cai, Y. Du, D. Wu, S. Gao, C. Tan, Z. Li, M. Ren, T. Osipowicz, S. Chen, Z. Jiang, J. Li, Y. Huang, J. Yang, Y. Chen, C. Y. Ang, Y. Zhao, P. Wang, L. Song, X. Wu, Z. Liu, A. Borgna, H. Zhang, Lithiation-induced amorphization of $Pd_3P_2S_8$ for highly efficient hydrogen evolution. *Nat. Catal.* **1**, 460–468 (2018).
92. X. Kong, K. Xu, C. Zhang, J. Dai, S. Norooz Oliaee, L. Li, X. Zeng, C. Wu, Z. Peng, Free-standing two-dimensional Ru nanosheets with high activity toward water splitting. *ACS Catal.* **6**, 1487–1492 (2016).
93. L. Wang, X. Duan, X. Liu, L. Gu, R. Si, Y. Qiu, Y. Qiu, D. Shi, F. Chen, X. Sun, J. Lin, J. Sun, Atomically dispersed Mo supported on metallic Co_9S_8 nanoflakes as an advanced noble-metal-free bifunctional water splitting catalyst working in universal pH conditions. *Adv. Energy Mater.* **10**, 1903137 (2020).
94. J. Lai, S. Li, F. Wu, M. Saqib, R. Luque, G. Xu, Unprecedented metal-free 3D porous carbonaceous electrodes for full water splitting. *Energ. Environ. Sci.* **9**, 1210–1214 (2016).
95. P. Li, X. Duan, Y. Kuang, X. Sun, Iridium in tungsten trioxide matrix as an efficient bi-functional electrocatalyst for overall water splitting in acidic media. *Small* **17**, 2102078 (2021).
96. Z. Zhuang, Y. Wang, C. Q. Xu, S. Liu, C. Chen, Q. Peng, Z. Zhuang, H. Xiao, Y. Pan, S. Lu, R. Yu, W. C. Cheong, X. Cao, K. Wu, K. Sun, Y. Wang, D. Wang, J. Li, Y. Li, Three-dimensional open nano-netcage electrocatalysts for efficient pH-universal overall water splitting. *Nat. Commun.* **10**, 4875 (2019).
97. H. You, D. Wu, Z. Chen, F. Sun, H. Zhang, Z. Chen, M. Cao, W. Zhuang, R. Cao, Highly active and stable water splitting in acidic media using a bifunctional iridium/cucurbit[6]uril catalyst. *ACS Energy Lett.* **4**, 1301–1307 (2019).
98. Q. Li, J. Li, J. Xu, N. Zhang, Y. Li, L. Liu, D. Pan, Z. Wang, F. L. Deepak, Ultrafine-grained porous Ir-based catalysts for high-performance overall water splitting in acidic media. *ACS Appl. Energy Mater.* **3**, 3736–3744 (2020).
99. H. Hu, F. M. D. Kazim, Z. Ye, Y. Xie, Q. Zhang, K. Qu, J. Xu, W. Cai, S. Xiao, Z. Yang, Electronically delocalized Ir enables efficient and stable acidic water splitting. *J. Mater. Chem. A* **8**, 20168–20174 (2020).
100. J. Zhang, G. Wang, Z. Liao, P. Zhang, F. Wang, X. Zhuang, E. Zschech, X. Feng, Iridium nanoparticles anchored on 3D graphite foam as a bifunctional electrocatalyst for excellent overall water splitting in acidic solution. *Nano Energy* **40**, 27–33 (2017).
101. L. Fu, G. Cheng, W. Luo, Colloidal synthesis of monodisperse trimetallic IrNiFe nanoparticles as highly active bifunctional electrocatalysts for acidic overall water splitting. *J. Mater. Chem. A* **5**, 24836–24841 (2017).
102. Z. Wang, Z. Zheng, Y. Xue, F. He, Y. Li, Acidic water oxidation on quantum dots of IrO_x/graphdiyne. *Adv. Energy Mater.* **11**, 2101138 (2017).

Acknowledgments: This work was partly supported by the Collaborative Innovation Center of Suzhou Nano Science and Technology. We thank beamline BL14W1 (Shanghai Synchrotron Radiation Facility) for providing the beam time. **Funding:** This work was financially supported by the National Key R&D Program of China (2020YFB1505802), the Ministry of Science and

Technology of China (2017YFA0208200 and 2016YFA0204100), the National Natural Science Foundation of China (22025108, 22121001, 21903058, 22105146, 51802206, 21875137, 51521004, and 51420105009), the Natural Science Foundation of Jiangsu Higher Education Institutions (17KJB150032 and BK20190810), the project of scientific and technologic infrastructure of Suzhou (SZS201708), Jiangsu Province High-Level Talents (JNHB-106), the Priority Academic Program Development of Jiangsu Higher Education Institutions (PAPD), Guangdong Provincial Natural Science Fund for Distinguished Young Scholars (2021B1515020081), startup support from Xiamen University, the Innovation Program of Shanghai Municipal Education Commission (project no. 2019-01-07-00-02-E00069), the 111 Project (project no. B16032), the Center of Hydrogen Science and Joint Research Center for Clean Energy Materials from Shanghai Jiao Tong University, and Guangzhou Key Laboratory of Low Dimensional Materials and Energy Storage Devices (20195010002). T.C. and H.Y. are supported by grants from startup supports of Soochow University and the Program for Jiangsu Specially-Appointed Professors (T.C.). H.Y. thanks the China Postdoctoral Science Foundation (2019 M660128) for financial support. **Author contributions:** X.H. and Y.X. conceived and supervised the research. X.H., Y.X., and J.W. designed the experiments. X.H., J.Wa., L.L., and Q.S. performed most of the experiments and data analysis. X.H., J.Wa., L.L., and Q.S. participated in various aspects of the experiments and discussions. J.Wu and F.L. performed TEM experiments. T.C. and H.Y. performed the DFT simulations. X.H., Y.X., J.Wa. and H.Y. wrote the paper. All authors discussed the results and commented on the manuscript. **Competing interests:** The authors declare that they have no competing interests. **Data and materials availability:** All data needed to evaluate the conclusions in the paper are present in the paper and/or the Supplementary Materials.

Submitted 13 August 2021
Accepted 7 January 2022
Published 2 March 2022
10.1126/sciadv.abl9271